Expanding the reach of diffusing wave spectroscopy and tracer bead microrheology

M. Helfer, C. Zhang, and F. Scheffold*
Department of Physics, University of Fribourg, Chemin du musée 3, 1700 Fribourg, Switzerland

(Received 30 January 2025; accepted 12 October 2025; published 9 December 2025)

Diffusing wave spectroscopy (DWS) is an extension of standard dynamic light scattering, applied to soft materials that are turbid or opaque. The propagation of light is modeled using light diffusion, characterized by a light diffusion coefficient that depends on the transport mean free path ℓ^* of the medium. DWS is highly sensitive to small particle displacements or other local fluctuations in the scattering properties and can probe subnanometer displacements. Analyzing the motion of beads in a viscoelastic matrix, known as one-bead microrheology, is one of the most common applications of DWS. Despite significant advancements since its invention in the late 1980s, including two-cell and multispeckle DWS, challenges such as merging single- and multispeckle data and limited accuracy for short correlation times persist. Here, we address these issues by improving the two-cell echo DWS scheme. We propose a calibration-free method to blend and merge echo and two-cell DWS data and demonstrate the use of an exponential basis fit to enhance data quality, in particular at very short times. Building on this, we introduce stable corrections for bead and fluid inertia, significantly improving the quality of microrheology data at high frequencies.

DOI: 10.1103/k34t-ghws

I. INTRODUCTION

Diffusing wave spectroscopy (DWS) is a standard light scattering technique used to study the dynamics of colloids, colloid-polymer mixtures, surfactant solutions, and other soft matter systems that display interesting complex relaxation dynamics [1–13]. Introduced in the late 1980s [14,15], DWS is an extension of the standard dynamic light scattering (DLS) approach [16]. In contrast to DLS, it is applied to materials that are turbid or opaque. In such materials, light is not scattered only once, as is the case in DLS, but multiple times. The propagation of light is often modeled using light diffusion characterized by a light diffusion coefficient that depends on the transport mean free path ℓ^* of the medium. Coherent light becomes dephased due to the motion of the scatterers in the medium [17–19], which can be quantified by analyzing the intensity time autocorrelation function (ICF) of the scattered light, analogously to the case of DLS.

DWS is commonly applied to samples such as dense suspensions and emulsions [11,12,20–24]. Alternatively, it can be applied to transparent samples by adding tracer beads that sense the dynamic environment of the medium [5,7,13,22,25–29]. The advantage of DWS over DLS is that it can be applied to turbid media that are not accessible to classical DLS, in regimes where multiple scattering suppression techniques such as three-dimensional cross-correlation fail [30]. Additionally, DWS is more sensitive than DLS to small particle displacements or other local fluctuations in the scattering properties. DWS can probe subnanometer displacements, as demonstrated by Weitz *et al*. in 1989 shortly after the method was introduced [31]. The high sensitivity of DWS is especially useful when tracer beads are embedded in a viscoelastic medium of interest. DWS can measure viscoelastic solids with elastic moduli of up to 100 kPa [28,32] and can study relaxations on microsecond timescales, such as Rouse-Zimm and bending modes of polymer dynamics [6,7,33].

Analyzing the motion of beads in a viscoelastic matrix is known as (single) bead microrheology [5,26,28], which is one of the most common applications of DWS. Pioneering work by Mason, Weitz, and others showed that the mean squared displacements (MSDs) of beads $\langle \Delta \vec{r}^2(t) \rangle$ can be directly converted into the linear viscoelastic spectrum, or complex modulus $G^*(\omega) = G'(\omega) + iG''(\omega)$, of the materials if the radius of the beads is known [25,34,35]. DWS provides access to this information from submicrosecond timescales to seconds and minutes, opening opportunities in rheology to study viscoelastic moduli over an enormous range of frequencies with a single measurement [7]. Many reviews of the theory underlying the method, along with numerous examples of its applications, have been published. We refer the reader to the literature for further details [1,3–5,13,27,28].

Since the invention of DWS, several substantial improvements have been made to the method. The original approach relied on time averages of the ICF, which requires the sample to be in a liquid state. Two-cell DWS, introduced in 2000 [17,36], and other ensemble averaging approaches [37–39] provided access to short correlation times for solid nonergodic systems. Multispeckle DWS, using either a camera or the echo scheme, was introduced in the early 2000s and provides access to longer correlation times for highly viscous or viscoelastic

*Contact author: Frank.Scheffold@unifr.ch

Published by the American Physical Society under the terms of the Creative Commons Attribution 4.0 International license. Further distribution of this work must maintain attribution to the author(s) and the published article's title, journal citation, and DOI.

solids such as glasses and gels [40–47]. In 2017, an automated method was developed to determine the mean free paths of optical transport and absorption for absorbing and nonabsorbing samples [29]. These advancements have made it possible to access the ICF over a range from typically 10 ns to tens of seconds or more, while keeping the measurement time on the order of a few minutes. Only when studying even longer relaxation times does the measurement time need to be further increased.

Despite these significant advances, shortcomings in the implementation of these methods can still lead to errors or reduced data quality. Moreover, access to very short correlation times is hindered by photon shot noise and the need to normalize the ICF, which, in its current implementation, introduces bias.

In the present work, we address these problems and propose two substantial improvements to the implementation of the two-cell echo DWS measurement scheme, which is the most common implementation of DWS. We present a calibration-free method to blend and merge echo and two-cell DWS measurements. Additionally, we demonstrate that using an exponential basis fit directly to the ICF can substantially improve the quality of the data. On the basis of this approach, we further demonstrate that a full correction for the bead and fluid inertia can be applied in a stable manner, further enhancing the microrheology data quality in the important high-frequency regime.

We note that a different approach, diffuse correlation spectroscopy using fast single-photon avalanche diode (SPAD) arrays, has made substantial progress over the past decade. The pixel count of such arrays has increased markedly and, although costs remain high, they have decreased significantly. Sie *et al.* [48,49] demonstrated multispeckle diffuse correlation spectroscopy with a 64×64 SPAD array comprising 4096 pixels and a temporal resolution of 4 μs, while Wayne *et al.* reported a 500×500 SPAD camera achieving a full-frame temporal resolution of 10 μs. Although not yet widely available and still under development, the SPAD approach is becoming increasingly competitive.

II. METHOD

Conventional photon correlation spectroscopy, as used in DLS or DWS, is based on the time-averaged photon correlation function recorded by a single-photon detector and processed using a hardware electronic or software correlator [16]. Echo DWS employs a multispeckle detection scheme to accurately measure the correlation function also in the presence of slow relaxation dynamics, typically for times equal to or longer than tenths of a second. Multispeckle DWS is achieved by illuminating an optical diffuser (e.g., ground glass) with a laser and then spinning or oscillating the glass at the desired frequency $1/\tau^{\mathrm{Echo}}$ [43,45]. The modulated speckle beam is used to illuminate the sample of interest. We use the following notation:

(i) $g_2(t)$: the DWS transmission ICF of the sample;

(ii) $g_2^{\mathrm{TC}}(t)$: the ICF measured in a two-cell (TC) configuration, where a slowly moving diffuser ('second cell' is placed in the beam path together with the sample;

(iii) $g_2^{\mathrm{Echo}}(t)$: the ICF obtained from correlation echoes recorded with a rotating or oscillating diffuser with period τ^{Echo}; and

(v) $g_2^{\mathrm{2nd}}(t)$: the two-cell ICF for a solid sample, where $g_2(t) \equiv 2$, and a slowly moving diffuser. The decay time τ_{TC} is controlled by the second cell motion.

In a typical experiment, the properly averaged echo correlation function is combined with a two-cell DWS measurement [17,36,42], where the ground glass is slowly displaced to force the decay of the ICF of the sample on a typical timescale τ_{TC}. These approaches ensure proper ensemble averaging, achieved by illuminating the sample with a larger number of different speckle fields. Both measurements are then combined to obtain a single ICF spanning correlation times from typically 12.5 ns to 10 s or more, covering an impressive nine orders of magnitude in relaxation times. However, the method, as it is currently used, suffers from two main limitations, both of which we address here.

A. Blending and merging the two-cell and echo signals

The shortest time accessible to Echo DWS is determined by the periodicity of the rotation or oscillation of the diffuser. Since this requires mechanical oscillation or rotation of an object weighing a few grams with high precision, the minimum accessible echo time is currently limited to just under a tenth of a second. Realizing somewhat shorter times is possible, but the procedure tends to be less stable and more prone to drift, requires more startup time for stabilization, or requires more complex and expensive equipment to provide the required accuracy. In this study, we used an already elevated frequency of 25 Hz, corresponding to the first echo located at $\tau^{\mathrm{Echo}} = 0.04$ s. Commercial instrumentation, such as the DWS RheoLab (LS Instruments, Switzerland), typically operates with echo correlation times that start at 0.1 s.

To be able to merge the Echo DWS and the two-cell DWS intensity correlation functions, $g_2(t) - 1$, the forced decay of the latter must be set to a time similar to or greater than τ^{Echo}. For comparison, in the original two-cell DWS study by Romer *et al.* [36], the value of τ_{TC} was six times greater than the final data point reported for $g_2(t) - 1$. Using the multiplication rule proposed in Ref. [17], the relation

$$g_2^{\mathrm{TC}}(t) - 1 = (g_2(t) - 1) \times \left(g_2^{\mathrm{2nd}}(t) - 1\right) \tag{1}$$

can be applied to the two-cell data. By dividing the measured $g_2^{\mathrm{TC}}(t) - 1$ by $g_2^{\mathrm{2nd}}(t) - 1$, we recover the true intensity correlation function $g_2(t) - 1$, where $g_2^{\mathrm{2nd}}(t) - 1$ is obtained independently through a long calibration measurement on a solid reference sample, such as a slab made of Teflon or colloidal beads embedded in a solid epoxy matrix. We note that for clarity, in this section we ignore the influence of the experimental coherence factor β and set it to 1.

The maximum time to which the true intensity correlation function can be reliably extracted from TC-DWS depends on the precision of the division based on Eq. (1). Unfortunately, the accuracy is often not very high, primarily due to the limited time available to average during the recording of $g_2^{\mathrm{TC}}(t) - 1$. For example, for $\tau_{\mathrm{TC}} = 0.3$, with a total measurement time of 300 s, this implies that the time average of $g_2^{\mathrm{TC}}(t) - 1$ covers $\sim 300/0.3 = 1000$ statistically independent speckle

realizations. The statistical noise scales as $1/\sqrt{1000} \simeq 3\%$ [50]; see also Table S1 in the Supplemental Material [51]. Thus, in practice, the forced decay of $g_2^{\mathrm{TC}}(t) - 1$ exhibits significant variations, and dividing by the measurement of the reference sample, $g_2^{\mathrm{2nd}}(t) - 1$, frequently results in visible perturbations of the ICF around τ^{Echo}. Moreover, if $g_2(t) - 1$ is joined with $g_2^{\mathrm{Echo}}(t) - 1$ at τ^{Echo} without data overlap, any deviation of the experimental $g_2(t) - 1$ from the properly ensemble-averaged value leads to a noticeable kink in the final correlation function used for further analysis; see also Fig. S1 in the Supplemental Material [51]. If data overlap is to be achieved using the standard approach, one would need to increase τ_{TC}, requiring a manifold extension of the measurement time, which is not practical.

Here, we propose an alternative approach based on dividing the measured correlation function by the echo correlation function. The latter is, up to a prefactor A, proportional to the true correlation function. Furthermore, the echo-ensemble average is generally accurate due to the large number of independent realizations probed during a single echo interval [43]. Thus,

$$\frac{g_2^{\mathrm{TC}}(t) - 1}{g_2^{\mathrm{Echo}}(t) - 1} = A\left(g_2^{\mathrm{2nd}}(t) - 1\right) = Ae^{-(t/\tau_{\mathrm{TC}})^p}. \tag{2}$$

The decay caused by the second cell, $g_2^{\mathrm{2nd}}(t) - 1$, is modeled as an exponential function, $e^{-(t/\tau_{\mathrm{TC}})^p}$. Due to the unidirectional motion of the diffuser $p = 2$ and $\tau_{\mathrm{TC}} = \mathrm{const.}$, see Fig. S4 in the Supplemental Material [51]. However, for finite measurement times, both values, A and p, can fluctuate around the mean value. For the examples shown in the main text that study a viscoelastic liquid, we find that $p = 2 = \mathrm{const}$ can be used, while for the viscoelastic solid reported in the Supplemental Material [51], fluctuations in p become noticeable, and therefore both τ_{TC} and p have to be treated as adjustable parameters.

Using this procedure, we obtain an effective second-cell decay characteristic of the measurement we carried out, removing the need for a calibration sample. We extract A and τ_{TC} from a fit to the data over, e.g., six data points, and then use τ_{TC} to correct $g_2^{\mathrm{TC}}(t) - 1$ and A to adjust the amplitude of $g_2^{\mathrm{Echo}}(t) - 1$. Finally, we combine the data over the fitting region and then append the remaining data points from the echo measurement. This approach ensures a smooth crossover between the two measurements without discontinuities.

B. Analysis of the short-time correlation function decay

One of the key features of DWS is the ability to measure tiny displacements of particles or other local rearrangements. DWS enables measurements of subdiffusive motion on nanometer length scales using visible light as a probe. In DWS-based microrheology, relaxations on (sub)microsecond timescales correspond to frequencies in the viscoelastic spectra of 10^6 rad/s and above, which no other laboratory technique can measure. For comparison, piezo-driven squeeze-flow devices can reach frequencies up to approximately 10^4 rad/s [52]. Torsional resonance oscillators extend the accessible frequency range into the 10^5 rad/s regime [53]; however, rheological measurements at such high frequencies are often limited by experimental constraints and are therefore impractical in most routine applications. Displacements of particles on these time scales are sub-Brownian, which means they are increasingly affected by the finite inertia of the tracer particles or beads and the surrounding fluid, which we will discuss in the next section. First, we focus on the accurate measurement of the short-time decay. DWS provides $[k(L/\ell^*)]^2\langle\Delta\vec{r}^2(t)\rangle$ over a specific range determined by the precision of the measurement, where $k = 2\pi n/\lambda$ is the wave number of scattered light in the host medium with a refractive index n. By increasing the optical density L/ℓ^* of the sample—either by increasing the cell thickness L or by lowering ℓ^* through an increase in the concentration of tracer beads—one can shift the window of accessible mean squared displacements to smaller values (and shorter timescales). However, this comes at the expense of reduced sensitivity to larger displacements.

For $t \to 0$, the ICF tends to a constant value of $g_2(0) - 1 = \beta$, where $\beta \lesssim 1$ denotes the coherence factor of the detection fiber optics and $\beta + 1$ corresponds to the zero-time *intercept* of the ICF. In a typical DWS microrheology experiment, for short relaxation times up to some tens or hundreds of microseconds, the bead motion often leads to relatively minor decays of the measured ICF, often only by a few percent. Extracting $\langle\Delta\vec{r}^2(t)\rangle$ from these minor decays is strongly affected by the accuracy with which one can determine β and by the significant photon shot noise at short correlation lag times [54]. Normalization to determine β is usually performed by extrapolating the measured $g_2(t)$ to $t = 0$ using a linear or polynomial fitting function. Once β is known, the normalized ICF is used to determine, e.g., $\langle\Delta\vec{r}^2(t)\rangle$. This standard procedure suffers from two problems. First, the choice of the polynomial order used for the fit, as well as the time interval used for the fit of the data, influences the exact value of β obtained. Here, it is important to note that, due to the inertia of the beads and the fluid, the short-time dynamics is rather complex even for simple colloidal suspensions in water, and thus no simple temporal scaling of the mean squared displacement $\langle\Delta\vec{r}^2(t)\rangle$ can be assumed [20,31,55]. Second, since the raw ICF is normalized by β but is used as is for further analysis, the experimental shot noise is not removed. As a result, the data fluctuate around the mean and reach values greater than 1, which is unphysical and leads to invalid data points for the bead mean squared displacement $\langle\Delta\vec{r}^2(t)\rangle$, which introduces further bias. This, in turn, creates difficulties in extracting the rheological information and performing the inertia corrections discussed in the following section.

Intercept-adjusted exponential basis fit

To obtain a smooth representation of the experimental data, we approximate the electric field autocorrelation function $g_1(t)$ using a fit with fixed, logarithmically spaced decay times:

$$g_1(t) = \sum_i P_i\, e^{-t/\alpha_i}, \tag{3}$$

where the basis functions are exponentials with fixed decay times α_i, and the amplitudes $P_i \geqslant 0$ are determined by fitting. We employ N logarithmically spaced decay times defined as

$$\alpha_i = 10^{-7}\ \mathrm{s} \times e^{\frac{i-1}{u}},\ i = 1, \ldots, N, \tag{4}$$

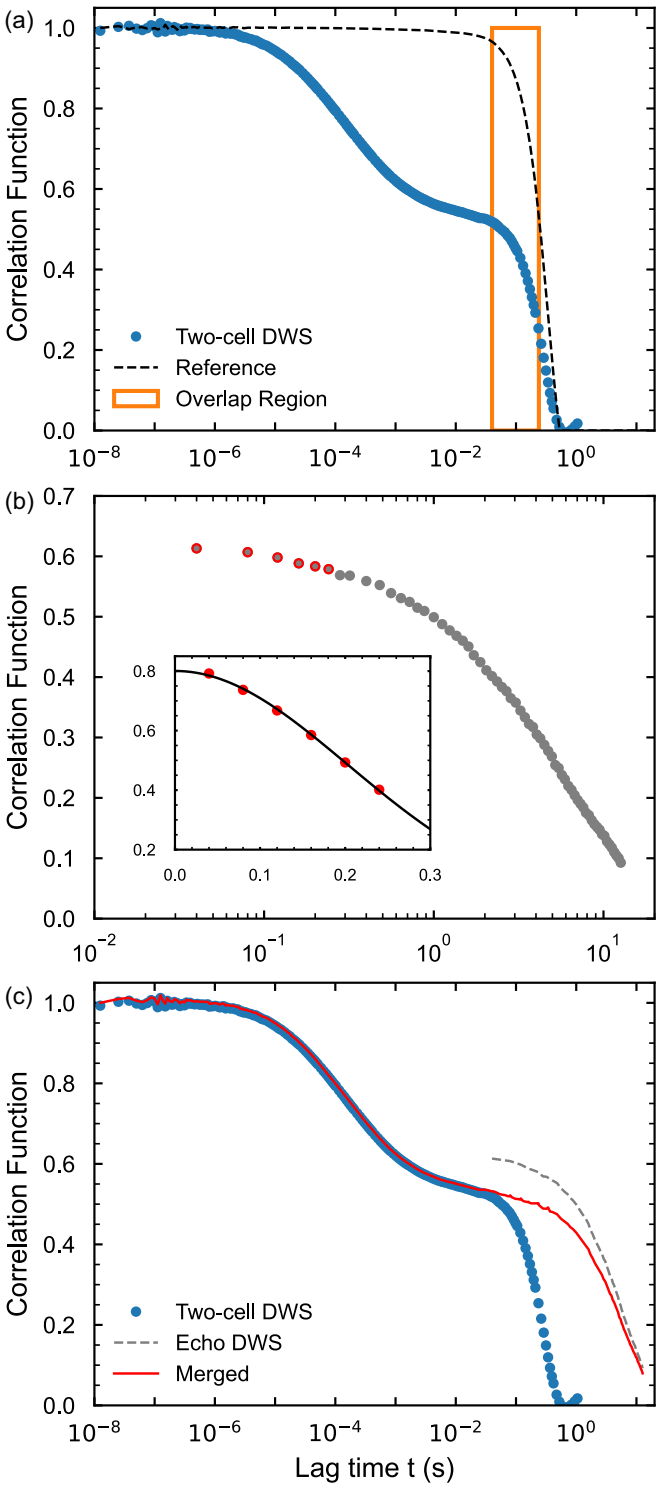


FIG. 1. (a) Two-cell correlation function $g_2^{\mathrm{TC}}(t) - 1$ recorded over 300 s for a wormlike micellar solution at $T = 20\,^{\circ}\mathrm{C}$ with polystyrene tracer beads embedded. The overlap region is marked with an orange line. The dashed line shows the correlation function measured for a solid piece of Teflon, recorded over 3 h and following Eq. (2) with $A = 0.988$ and $\tau_{\mathrm{TC}} = 0.298$ s. (b) Echo DWS for the same sample recorded over 60 s, with data up to 12 s. The oscillation period is $\tau^{\mathrm{Echo}} = 0.04$ s. Inset: Ratio of the two-cell correlation function to the echo correlation function. Line: Best fit to the data with $A = 0.800$ and $\tau_{\mathrm{TC}} = 0.287$ s using Eq. (2). (c) Blending and merging two-cell DWS and echo data. Blue open square: Two-cell correlation function. Dashed line: Echo correlation function. Red line: Merged correlation function obtained by multiplying the echo data by the parameter A and dividing the two-cell data by the exponential function [Eq. (2)] (up to $t = 6 \times \tau_{\mathrm{Echo}}$), and then merging the two datasets.

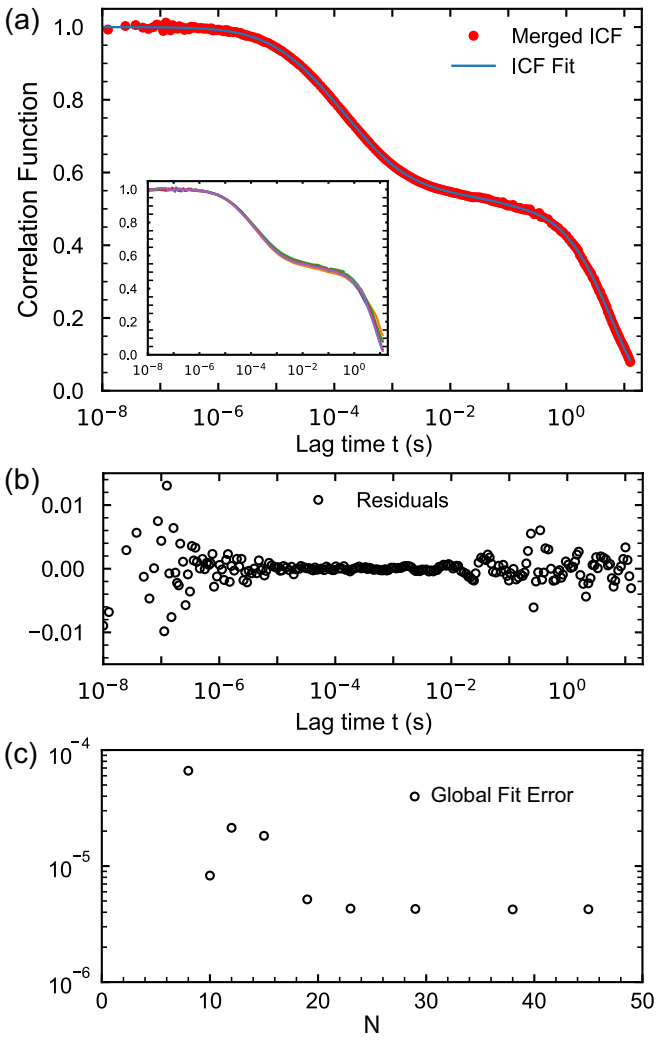


FIG. 2. (a) Fit to the intensity correlation function (ICF). Red circles: Merged correlation function $g_2(t) - 1$, as shown in Fig. 1(c). Blue line: Exponential basis fit $g_2^{\mathrm{fit}}(t)$ to the correlation function. The experimental data are normalized using the ICF fit extrapolated to $t = 0$. Inset: Five repetitions of the merged correlation function $g_2(t) - 1$, normalized using the exponential basis fit. (b) Open circles: Fit residuals $r(t) = g_2(t) - g_2^{\mathrm{fit}}(t)$. (c) Open circles: global fit error, Eq. (7), evaluated for different numbers of exponential terms N.

α_N is chosen to be one or two orders of magnitude larger than the time window of interest. Solving for u gives $u = (N-1)/\ln(\alpha_N/\alpha_0)$. For viscoelastic solid samples exhibiting a stable plateau, the fit can be further improved by including a constant offset term in Eq. (3).

Here, we use $N = 45$ and $u = 2$ ($\alpha_N = 360$ s) to ensure robustness, but tests with smaller values yield similar results

at a significantly lower computational cost as long as $N \geqslant 10$ [see Fig. 2(c)]. This exponential basis approach provides a stable and flexible reconstruction of $g_1(t)$, enabling an accurate representation even at very short times. Applying the Siegert relation, the intensity correlation function is modeled as

$$g_2(t) - 1 = \left(\sum_i P_i e^{-t/\alpha_i} \right)^2. \tag{5}$$

This formulation implicitly adjusts the intercept via

$$\beta + 1 = g_2(0) = 1 + \left(\sum_i P_i \right)^2 \tag{6}$$

and thus allows us to normalize the ICF, avoiding the need for separate normalization or intercept fitting. The fitting procedure minimizes the mean squared deviation between the modeled and measured ICFs:

$$\text{Error} = \frac{1}{N'} \sum_{j=1}^{N'} \left[\left(\sum_{i=1}^{N} P_i e^{-t_j/\alpha_i} \right)^2 - (g_2(t_j) - 1) \right]^2. \tag{7}$$

where $j = 1 - N'$ is the data-point index in the multiple-tau channel layout of the ICF, and N' is the total number of data points.

After obtaining the optimal weights P_i, the model is used to reconstruct a smoothed, intercept-corrected ICF:

$$g_2^{\text{fit}}(t) - 1 = \left(\sum_i P_i e^{-t/\alpha_i} \right)^2 \Big/ \left(\sum_i P_i \right)^2. \tag{8}$$

Finally, the mean square displacement (MSD) is extracted by numerically inverting this fitted correlation function using the full DWS model in transmission geometry, as given in Eq. (9).

We emphasize that this fitting procedure does not constitute an additional smoothing step in the DWS microrheology analysis; rather, it replaces the conventional smoothing fit applied to the mean-squared displacements [25], offering the advantages discussed above.

C. One-bead microrheology with inertia corrections

The time relaxation of the intensity correlation function (ICF) is determined by the motion of the beads and the light scattering process. Precise analytical formulas have been developed to extract the bead MSD from the measured DWS intensity autocorrelation functions in transmission geometry. The measured mean squared displacement, in turn, is determined by the linear viscoelastic properties of the host medium and, at short times, also by the inertia of the bead and the fluid. Particle interactions, convection or flow, and phase separation can also influence the particle motion, but these effects will not be discussed here [3,13]. Ignoring such effects, the analysis procedure proceeds as follows: First, we extract the MSD, $\langle \Delta \vec{r}^2(t) \rangle$, from the ICF. Next, we remove the contributions due to bead and fluid inertia to obtain the unperturbed viscoelastic spectra of the (complex fluid) host medium. The different steps and approximations made will be discussed below. In addition, we will highlight the importance of clean and low-noise data to stably perform this analysis.

1. Mean squared displacement

We first convert the experimental data to the MSD using Eq. (9) taken from Ref. [3], assuming that the slab thickness L, the sample's transport mean free path ℓ^*, and the wave number k are known. Since we study nonabsorbing samples, we neglect the effects of absorption, but these can be easily incorporated if required [29].

$$g_2(t) - 1 = \left\{ \frac{\frac{L/\ell^* + 4/3}{z_0/\ell^* + 2/3} \left(\sinh\left[\frac{z_0}{\ell^*} \sqrt{k^2 \langle \Delta \vec{r}^2(t) \rangle} \right] + \frac{2}{3} \sqrt{k^2 \langle \Delta \vec{r}^2(t) \rangle} \cosh\left[\frac{z_0}{\ell^*} \sqrt{k^2 \langle \Delta \vec{r}^2(t) \rangle} \right] \right)}{\left(1 + \frac{4}{9} k^2 \langle \Delta \vec{r}^2(t) \rangle \right) \sinh\left[\frac{L}{\ell^*} \sqrt{k^2 \langle \Delta \vec{r}^2(t) \rangle} \right] + \frac{4}{3} \sqrt{k^2 \langle \Delta \vec{r}^2(t) \rangle} \cosh\left[\frac{L}{\ell^*} \sqrt{k^2 \langle \Delta \vec{r}^2(t) \rangle} \right]} \right\}^2. \tag{9}$$

If internal reflections are absent or neglected, $z_0/\ell^* \simeq 2/3$. In our case, we consider a glass cuvette in air; thus, $z_0/\ell^* \simeq 2$, a value derived from the work of Durian and co-workers [56]. The larger L/ℓ^*, the less important the choice of z_0 becomes [13]. By numerical inversion of Eq. (9) for each value of t, we obtain a precise value of $\langle \Delta \vec{r}^2(t) \rangle$ for each value of $g_2^{\text{fit}}(t) - 1$, with no fitting or ambiguity involved in the process.

2. Microrheology routine

We use the following microrheology routine, based on Mason's work [57], to determine the apparent complex modulus (inertia affected) $Z^*(\omega)$ from the mean squared displacement data $\langle \Delta r^2(t) \rangle$, determined in the previous step, as follows:

$$\alpha(\omega) = \left. \frac{\mathrm{d} \ln \langle \Delta \vec{r}^2(t) \rangle}{\mathrm{d} \ln t} \right|_{t=1/\omega}, \tag{10}$$

$$i\omega F_\omega\{\langle \Delta \vec{r}^2(t) \rangle\} \approx \left\langle \Delta \vec{r}^2\left(\frac{1}{\omega} \right) \right\rangle \Gamma[1 + \alpha(\omega)] i^{-\alpha(\omega)}, \tag{11}$$

where t is substituted by $1/\omega$, and finally

$$Z^*(\omega) = \frac{k_B T}{\pi a \omega F_\omega\{\langle \Delta \vec{r}^2(t) \rangle\}}, \tag{12}$$

where a denotes the radius of the tracer beads. Equation (12) is also known as the generalized Stokes-Einstein equation (GSE) (in the Fourier domain) [28,57].

We note that Evans *et al.* developed a direct conversion algorithm from the MSD—or equivalently, from the creep compliance (see, e.g., Eq. (3.99) in Ref. [28])—to the storage and loss moduli [58,59]. This method circumvents the approximation used in Eq. (11). It was later refined by Tassieri *et al.* [59]. Figure S4 of the Supplemental Material [51] shows that our approach and the direct conversion yield nearly identical results. The method by Evans *et al.* tends to produce noisier

data, while the refined version by Tassieri *et al.* mitigates this issue by avoiding an approximation that can introduce artificial scatter [60]. Small residual differences remain, but a detailed analysis of these discrepancies lies beyond the scope of the present work and should be addressed in future studies.

3. Inertia correction

At very short times, the common description of thermal Brownian motion breaks down, a phenomenon that has been well known since Einstein's pioneering work on the subject in 1905 [61]. The transition from ballistic to Brownian dynamics, which is strongly affected by inertia and hydrodynamics, has attracted renewed attention more recently [62–65]. Neglecting these contributions in the microheology analysis can result in significant errors. Properly accounting for these effects at short times, corresponding to high frequencies (ω) when determining the complex modulus $G^*(\omega)$, enables the extraction of critical data that would otherwise be challenging or impossible to obtain.

The inertia correction formula used in the present study, Eq. (13), is based on the work of Domínguez-García *et al.* [66]. The complete theoretical treatment applied here was first developed and published by Schieber and co-workers [67]. Prior to that, an (iterative) approximative algorithm to correct for inertia effects was developed by one of us in Willenbacher *et al.* [7] and similarly employed by Mizuno *et al.* [68]. From the apparent complex modulus $Z^*(\omega)$, extracted from the experimental data, we calculate the complex modulus of the host medium as follows:

$$G^*(\omega) = Z^*(\omega) + \frac{m^*\omega^2}{6\pi a} + \frac{a^2\omega^2}{2}\left[\sqrt{\rho^2 - \frac{2\rho}{3\pi a^3}\left(\frac{6\pi a}{\omega^2}Z^*(\omega) + m^*\right)} - \rho\right]. \tag{13}$$

The effective mass of the tracer beads is

$$m^* = \frac{4\pi a^3}{3}\rho_b + \frac{2\pi a^3}{3}\rho, \tag{14}$$

where ρ_b is the bead density and ρ is the medium density in kg/m^3. The resulting $G^*(\omega)$ is a complex function, which can be evaluated using computational tools such as MATHEMATICA (Wolfram, USA) [69] or PYTHON (Python Software Foundation) [70]. We can then obtain the following:

(i) the absolute value $|G^*(\omega)|$;
(ii) the storage modulus $G'(\omega) = \mathrm{Re}\, G^*(\omega)$; and
(iii) the loss modulus $G''(\omega) = \mathrm{Im}\, G^*(\omega)$.

III. RESULTS—EXPERIMENTAL VALIDATION

A. Sample

We study DWS microrheology on a wormlike micellar sample discussed extensively in previous work [7,41,71,72]. To do this, we prepare an aqueous solution of cetylpyridinium chloride and sodium salicylate (100 mM CPyCl and 60 mM NaSal). We mix the sample with polystyrene beads with a diameter of 420 nm to a final concentration slightly below 1% in volume. We determine the transport mean free path ℓ^* using the commercial "DWS RheoLab" instrument (LS Instruments, Switzerland) [29] and, using Mie scattering theory, correct the obtained value for the slight mismatch in laser wavelength. We prepare the sample such that the micellar concentration relative to the aqueous solvent phase is kept constant. The sample displays nearly perfect Maxwellian behavior at low frequencies or slow relaxation times and exhibits the characteristic dynamics of polymer relaxations at short times. It is a strongly viscoelastic liquid with a terminal relaxation time that reacts to temperature over a wide range. Here, we use it as a model system to demonstrate our improved implementation of two-cell echo diffusing wave spectroscopy for different terminal relaxation times larger than or comparable to τ^{TC}.

B. Experimental setup

We carry out DWS experiments in transmission geometry, where an expanded incident laser beam illuminates the sample contained in a rectangular glass cuvette, with a width larger than its thickness L. The diffusely scattered light is recorded on the opposite side, in transmission, using a single-mode optical fiber. We use a classical custom-made DWS setup with a helium-neon gas laser operating at a 632.8 nm wavelength emission. The collimated laser beam is directed toward a 12.5 mm diameter holographic diffusor (Edmund Optics, UK) with a 5° diffusing angle. Compared to ground- or opal-glass diffusers, holographic diffusers offer higher light transmission and a more even distribution of light. They provide control over the diffusion angle, eliminating the need for an additional collimation lens between the diffuser and the sample. In our setup, the diffusor is mounted on a Voice Coil Actuated Flexure Scanner (VCFL35, Thorlabs, USA). The scanner is operated at 25 Hz using a function generator. The light diffracted from the diffusor in the forward direction forms a random speckle field that we use to illuminate the sample cuvette. The sample is contained in a 12.5 mm wide (10 mm inner width) glass cuvette (Hellma, Germany) with a path length of $L = 2$ mm. For the distance chosen for the ground glass from the cuvette (a few centimeters), the speckle beam size is comparable in width to that of the cuvette. We place a black circular aperture with an 8 mm opening in front of the cuvette to avoid illuminating the edges of the cuvette.

The light transmitted through the multiple scattering sample is detected in the far field on the other side using a single-mode fiber (OZ Optics, Canada). The single-mode fiber is split 50/50 and each arm is connected to an APD single-photon detector (Excelitas, USA). Using a digital correlator (LS Instruments, Switzerland), we calculate the pseudo-cross-correlation function of the scattered photons, which is equal to the photon autocorrelation function, but eliminates detector noise (also known as afterpulsing effects). The setup is similar to the one shown in Fig. 1 of Ref. [43].

We operate the voice coil scanner in two modes. In slow mode, ground glass motion leads to a slow decay of the ICF on a timescale of τ^{TC} but does not affect the short-time dynamics except for providing adequate ensemble averaging of the correlation function [Fig. 1(a)]. We record the ICF using the standard multiple tau channel layout (LS Correlator, LS Instruments, Switzerland). We perform an approximate normalization of $g_2^{\mathrm{TC}}(t) - 1$ by dividing the data by the

values recorded around $t = 10^{-7}$ s, which typically range between 0.9 and 0.95. In fast mode, the periodic oscillation of the ground glass with a period of $\tau^{\text{echo}} = 0.04$ s leads to correlation echoes [43–45], which we detect using the linear correlator scheme configured in the digital correlator. This scheme provides a time resolution of 1 μs and spans 16 channels centered around $\tau^{\text{echo}} = 0.04$ s and multiples thereof. From a Lorentzian fit of the detected correlation echoes, we determined the total echo area—shown in Fig. 1(b) rescaled by an arbitrary constant—which gives a robust measure of the intensity correlation function, up to an undetermined prefactor [43,44]. The measurement times for the slow mode were 300 s and 60 s for the fast (echo) mode.

C. Merging two-cell DWS and echo data

We first generate an interpolation function for $g_2^{\text{TC}}(t) - 1$ with SciPy based on the data recorded using a multiple tau layout of correlation lag times [73]. SciPy employs piecewise polynomial interpolation (cubic interpolation for smoothness) to construct the interpolating function [74]. This function is then used to calculate the values of $g_2^{\text{TC}}(t) - 1$ at $t = \tau^{\text{echo}}$ and its multiples in the linear lag time scheme of the echo correlation function. To merge the two datasets, we use the first six echo data points from $t = \tau^{\text{echo}} = 0.04$ s to $t = 6\tau^{\text{echo}} = 0.24$ s. The choice of six is *ad hoc*, but it is evident that at least a few overlapping data points are necessary to blend the two measurements effectively, while selecting an excessively large number of overlapping points provides little benefit. For these six points $i = 1, 2, .., 6$, we calculate the ratio $[g_2^{\text{TC}}(i \times \tau^{\text{Echo}}) - 1]/[g_2^{\text{Echo}}(i \times \tau^{\text{Echo}}) - 1]$. As shown in the inset of Fig. 1(b), we find that for $\tau^{\text{Echo}} \simeq 0.04$ s and our choice of $\tau^{\text{TC}} \simeq 0.29$ s, this range of data points is well described by Eq. (2), and we extract the parameters A and τ_{TC} from a fit to the data. Finally, we multiply the full dataset for $g_2^{\text{Echo}}(t) - 1$ by A, divide the dataset $g_2^{\text{TC}}(t) - 1$ by $e^{-(t/\tau_{\text{TC}})^2}$, and truncate it at $t = 6\tau^{\text{echo}} = 0.24$ s. We merge both datasets into one, and the result is shown as a red line in Fig. 1(c). Our results suggest that as long as $\tau_{\text{TC}} \geqslant 6\tau^{\text{Echo}}$, corresponding to a second-cell ICF decay of no more than $1/e$ for the last overlapped data point, the parameters A and τ_{TC} can be extracted accurately and the data can be seamlessly blended and merged. We note that the blending and merging approach introduced here could equally be applied when combining two-cell DWS with camera-based DWS to cover the slow relaxation time window, as discussed in Refs. [40,41].

D. DWS microrheology and inertia correction

1. Data preparation

In the previous section, we demonstrated how to blend and merge two-cell and echo measurements without the need for a calibration sample, achieving a smooth and steady transition between the two datasets. We note that the first few echo data points are relatively widely spaced on the time axis, but they are now combined with the two-cell data over the same time range and instead form a fairly dense dataset. Echo data at larger times are densely spaced compared to the multiple-tau channel layout. This outcome is important, as the MSD of the particles is typically represented in logarithmic format, and microrheology routines often rely on analyzing derivatives of the logarithm of the mean squared displacement, Eq. (10). An unevenly spaced distribution of time channels around τ^{Echo} can introduce errors and inconsistencies in data processing.

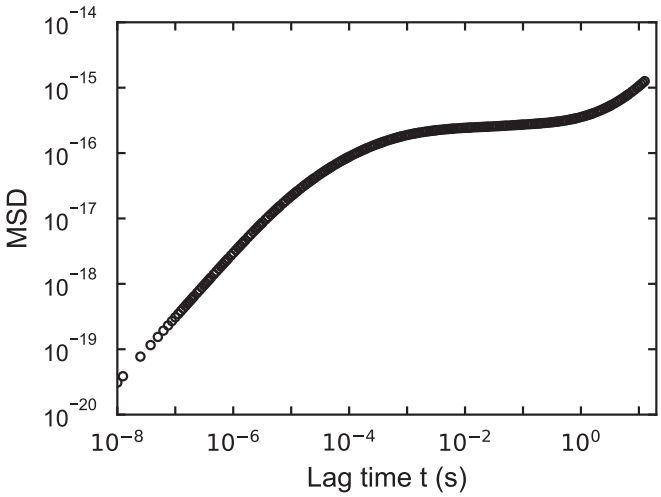


FIG. 3. Open black circles: Mean squared particle displacement calculated from the intensity correlation function via Eq. (9).

2. Fitting and smoothing

We use the merged dataset as input for the exponential basis fit (Sec. II B 1). Our primary objective is to achieve a minimally biased extrapolation to $t = 0$ and smooth data, enabling the application of the inertia correction and the microrheology algorithm. Using the SciPy interpolation function, we remap the data onto the original multiple-tau channel layout of the digital correlator to prevent oversampling and undue weighting of the longer-time data. The merged dataset and the fit $g_2^{\text{fit}}(t) - 1$ are shown in Fig. 2(a) together with the residuals [Fig. 2(b)]. In the inset of Fig. 2(a), we show five repetitions of the same experiment to demonstrate its stability and reproducibility; see also Table S1 in the Supplemental Material [51]. We note that without this step, applying the inertia correction using Eq. (13) would not be feasible without either discarding the high-frequency data of interest or manually adjusting the normalization and smoothing the short-time data, as done in earlier work [7,66].

3. Microrheology

We determine the transport mean free path of the samples to $\ell^* \simeq 330$ μm which, together with the known values of $L = 2$ mm and $k = \frac{2\pi n}{\lambda} = 13.2\,\mu\text{m}^{-1}$, for $n_{\text{water}} = 1.33$ is needed to extract the particle mean squared displacement $\langle \Delta r^2(t) \rangle$ using Eq. (9) and the data are shown in Fig. 3.With knowledge of the radius of the beads ($a = 210$ nm), we determine the apparent complex modulus $Z^*(\omega)$ using Eq. (12) and the result is shown in Fig. 4(a). Finally, we apply Eq. (13) to account for the fluid and bead inertia, obtaining the true moduli of the sample, shown in Fig. 4(b); see also Fig. S2 in the Supplemental Material [51]. The following values are used: $\rho_b = 1050\,\text{kg/m}^3$ (polystyrene bead mass density) and

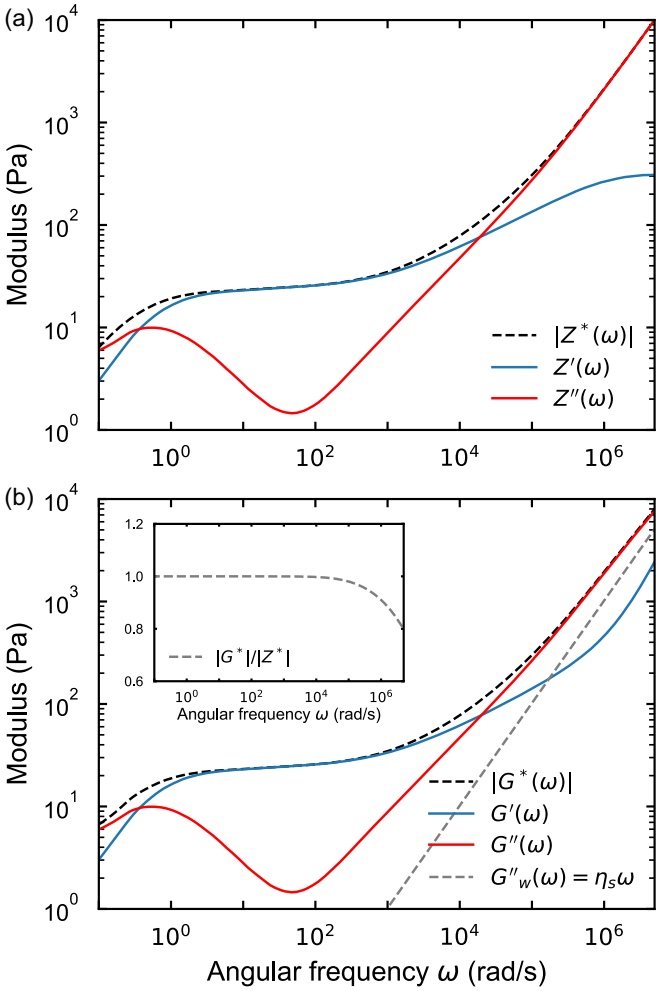


FIG. 4. (a) Apparent complex moduli of the micellar solution $Z^*(\omega)$ at $T = 20\,^\circ$C, as well as the real and the imaginary parts $Z'(\omega), Z''(\omega)$, obtained using the generalized Stokes-Einstein relation, Eq. (12), and Mason's routine to convert the mean squared displacement [57]. (b) Corrected complex modulus of the sample after accounting for bead and fluid inertia, which primarily affects data at frequencies $\omega \geqslant 10^5$ rad/s. The solvent loss modulus $G''(\omega) = \eta_s\omega$ is shown as a dashed line. The data are truncated at $\omega = 5 \times 10^6$ rad/s. The inset in panel (b) shows the ratio of uncorrected and corrected moduli $|G^*|/|Z^*|$.

$\rho \simeq 1000\,\mathrm{kg/m^3}$ (medium density) and temperature-dependent water viscosity η_s [75].

In the high-frequency limit, we truncated the data at $\omega \simeq 5 \times 10^6$ rad/s, above which the ICF decays by less 0.5% from 1 to 0.995. Using a larger L/ℓ^* leads to a faster decay and may provide access to even higher frequencies. However, as seen in Fig. 4(b), the complex modulus gradually approaches the modulus of the solvent $G''(\omega) = \eta_s\omega$. Thus, the upper bound for a stable DWS high-frequency analysis remains to be determined and is likely to be system dependent. Using the improved DWS implementation, we are already pushing the boundaries of the technique. Still, both the blending and merging procedures and the inertia correction are stable, and the process is highly reproducible.

For a practical test, we apply our method to study the viscoelastic moduli by performing a temperature ramp (Fig. 5).

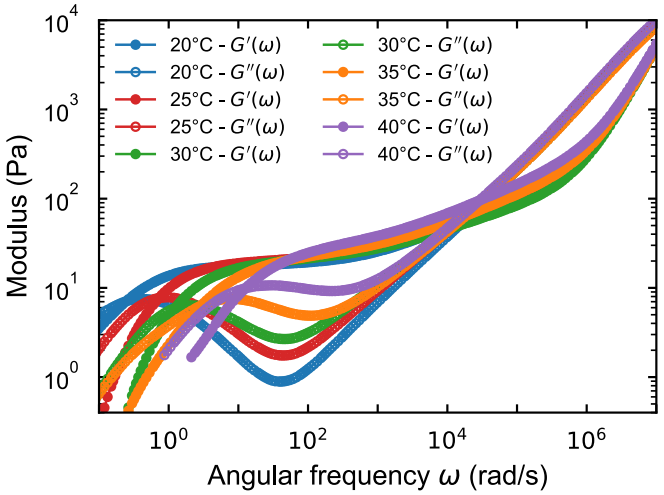


FIG. 5. Microrheology of the micellar solution at different temperatures, ranging from $T = 20\,^\circ$C to $T = 40\,^\circ$C, illustrating the improved two-cell echo diffusing wave spectroscopy and tracer bead microrheology.

Analogous experiments were reported earlier by Oelschlaeger *et al.*, and our data compare quantitatively to these literature data [72]. While the previously published data were truncated at $\omega \simeq 10^5$ rad/s, here we extend the frequency range reproducibly for all temperatures up to $\omega \simeq 5 \times 10^6$ rad/s. Finally, we also demonstrated the method on a viscoelastic solid sample (Figs. S5 and S6 in the Supplemental Material [51]). To this end, we studied a dense microgel suspension without added tracer beads. The system is identical to the one described in Ref. [76].

IV. CONCLUSIONS

In the present work, we presented an implementation of two-cell echo DWS aimed at significantly improving the data quality and stability and thus extending the reach of DWS and DWS-based tracer bead microrheology. We replaced the standard calibration method for two-cell DWS, introduced by Romer *et al.* in 2000 [36], later used by many others and implemented in commercial DWS equipment [13,29,42], with a calibration-free approach. This method generically corrects small fluctuations in the terminal decay time arising from imperfect temporal averaging, allowing for a seamless transition between two-cell DWS and echo DWS. This smooth transition, in turn, facilitates a stable conversion of the bead mean squared displacement to the complex viscoelastic modulus via the GSER. Combined with the normalization of the correlation function using the exponential basis fit and the elimination of shot noise, the quality of DWS data is substantially improved. This enhancement enables the routine application of published formulas to correct the effects of fluid and tracer bead inertia. As a result, the method provides unprecedented access to the high-frequency regime [7]. This capability will be beneficial for addressing questions related to the short-time dynamics of polymeric and other soft matter systems. Furthermore, this approach brings DWS closer to other advanced techniques, such as neutron spin echo spectroscopy, connecting the high-frequency viscoelastic

relaxations to submicrosecond-scale dynamics in systems like microgels [77] or protein hydrogels [78].

ACKNOWLEDGMENTS

We thank Erika Eiser (NTU Trondheim, Norway) and Andrea Vaccaro (LS Instruments, Switzerland) for valuable discussions. This work was financially supported by the Swiss National Science Foundation through Projects No. 10000141 and No. 10002524. We thank the referees for their constructive feedback, and in particular the second referee for helpful suggestions on improving the fitting of the ICF.

F.S. designed the study and wrote the original MATHEMATICA code. M.H. and C.Z. conducted the experiments. C.Z. designed the exponential basis fit. M.H. implemented and tested the PYTHON package (pyDWS). All authors participated in the data analysis. F.S. wrote the manuscript with contributions from all authors.

DATA AVAILABILITY

All experimental data and model output discussed in the manuscript have been uploaded to the repository Zenodo [79]. The source code for the pyDWS Python package can be found on GitHub/pyDWS [80] and can also be installed directly from PyPi/pyDWS [81]. All additional data sets generated and/or analyzed during the current study are available from the corresponding author upon reasonable request.

[1] D. Weitz, J. Zhu, D. Durian, H. Gang, and D. Pine, Diffusing-wave spectroscopy: The technique and some applications, Phys. Scr. **T49B**, 610 (1993).

[2] D. J. Pine, D. A. Weitz, J. Zhu, and E. Herbolzheimer, Diffusing-wave spectroscopy: Dynamic light scattering in the multiple scattering limit, J. Phys. **51**, 2101 (1990).

[3] D. J. Pine and D. A. Weitz, Diffusing-wave spectroscopy, in *Dynamic Light Scattering: The Method and Some Applications*, edited by W. Brown (Oxford University Press, Oxford, Wyn Brown, Uppsala, Sweden, 1993), pp. 652–720.

[4] G. Maret, Diffusing-wave spectroscopy, Curr. Opin. Colloid Interface Sci. **2**, 251 (1997).

[5] J. Harden and V. Viasnoff, Recent advances in DWS-based micro-rheology, Curr. Opin. Colloid Interface Sci. **6**, 438 (2001).

[6] B. R. Dasgupta, S.-Y. Tee, J. C. Crocker, B. Frisken, and D. Weitz, Microrheology of polyethylene oxide using diffusing wave spectroscopy and single scattering, Phys. Rev. E **65**, 051505 (2002).

[7] N. Willenbacher, C. Oelschlaeger, M. Schopferer, P. Fischer, F. Cardinaux, and F. Scheffold, Broad bandwidth optical and mechanical rheometry of wormlike micelle solutions, Phys. Rev. Lett. **99**, 068302 (2007).

[8] J. Galvan-Miyoshi, J. Delgado, and R. Castillo, Diffusing wave spectroscopy in Maxwellian fluids, Eur. Phys. J. E **26**, 369 (2008).

[9] Z. Fahimi, F. J. Aangenendt, P. Voudouris, J. Mattsson, and H. M. Wyss, Diffusing-wave spectroscopy in a standard dynamic light scattering setup, Phys. Rev. E **96**, 062611 (2017).

[10] Z. Xing, A. Caciagli, T. Cao, I. Stoev, M. Zupkauskas, T. O'Neill, T. Wenzel, R. Lamboll, D. Liu, and E. Eiser, Microrheology of DNA hydrogels, Proc. Natl. Acad. Sci. USA **115**, 8137 (2018).

[11] V. Lorusso, D. Orsi, F. Salerni, L. Liggieri, F. Ravera, R. McMillin, J. Ferri, and L. Cristofolini, Recent developments in emulsion characterization: Diffusing wave spectroscopy beyond average values, Adv. Colloid Interface Sci. **288**, 102341 (2021).

[12] K. A. Dennis, Q. Li, N. Sbalbi, S. C. Brown, and E. M. Furst, Diffusing wave spectroscopy measurements of colloidal suspension dynamics, Langmuir **40**, 6129 (2024).

[13] F. Scheffold, Light scattering and propagation in turbid media, in *Neutrons, X-rays, and light: Scattering Methods Applied to Soft Condensed Matter*, edited by P. Lindner and J. Oberdisse (Elsevier, France, 2024), pp. 581–610.

[14] G. Maret and P. Wolf, Multiple light scattering from disordered media. The effect of Brownian motion of scatterers, Z. Phys. B **65**, 409 (1987).

[15] D. J. Pine, D. A. Weitz, P. M. Chaikin, and E. Herbolzheimer, Diffusing wave spectroscopy, Phys. Rev. Lett. **60**, 1134 (1988).

[16] B. J. Berne and R. Pecora, *Dynamic Light Scattering: With Applications to Chemistry, Biology, and Physics* (Dover Publications, Inc. Mineoloa, New York, 2000).

[17] F. Scheffold, S. Skipetrov, S. Romer, and P. Schurtenberger, Diffusing-wave spectroscopy of nonergodic media, Phys. Rev. E **63**, 061404 (2001).

[18] D. A. Boas, L. Campbell, and A. G. Yodh, Scattering and imaging with diffusing temporal field correlations, Phys. Rev. Lett. **75**, 1855 (1995).

[19] D. A. Boas and A. G. Yodh, Spatially varying dynamical properties of turbid media probed with diffusing temporal light correlation, J. Opt. Soc. Am. A **14**, 192 (1997).

[20] X. Qiu, X. Wu, J. Xue, D. Pine, D. Weitz, and P. M. Chaikin, Hydrodynamic interactions in concentrated suspensions, Phys. Rev. Lett. **65**, 516 (1990).

[21] L. Rojas-Ochoa, S. Romer, F. Scheffold, and P. Schurtenberger, Diffusing wave spectroscopy and small-angle neutron scattering from concentrated colloidal suspensions, Phys. Rev. E **65**, 051403 (2002).

[22] Q. Li, K. A. Dennis, Y.-F. Lee, and E. M. Furst, Two-point microrheology and diffusing wave spectroscopy, J. Rheol. **67**, 1107 (2023).

[23] H. S. Kim, N. Şenbil, C. Zhang, F. Scheffold, and T. G. Mason, Diffusing wave microrheology of highly scattering concentrated monodisperse emulsions, Proc. Natl. Acad. Sci. USA **116**, 7766 (2019).

[24] Y. Xu and T. G. Mason, Jamming and depletion in extremely bidisperse mixtures of microscale emulsions and nanoemulsions, Sci. Adv. **9**, eadh3715 (2023).

[25] T. G. Mason and D. A. Weitz, Optical measurements of frequency-dependent linear viscoelastic moduli of complex fluids, Phys. Rev. Lett. **74**, 1250 (1995).

[26] M. L. Gardel, M. T. Valentine, and D. A. Weitz, Microrheology, in *Microscale Diagnostic Techniques* (Springer, Berlin, Heidelberg, 2004), pp. 1–49.

[27] T. A. Waigh, Microrheology of complex fluids, Rep. Prog. Phys. **68**, 685 (2005).

[28] E. M. Furst and T. M. Squires, *Microrheology* (Oxford University Press, Oxford, UK, 2017).

[29] C. Zhang, M. Reufer, D. Gaudino, and F. Scheffold, Improved diffusing wave spectroscopy based on the automatized determination of the optical transport and absorption mean free path, Korea-Aust. Rheol. J. **29**, 241 (2017).

[30] I. D. Block and F. Scheffold, Modulated 3D cross-correlation light scattering: Improving turbid sample characterization, Rev. Sci. Instrum. **81**, 123107 (2010).

[31] D. A. Weitz, D. J. Pine, P. N. Pusey, and R. J. A Tough, Nondiffusive Brownian motion studied by diffusing-wave spectroscopy, Phys. Rev. Lett. **63**, 1747 (1989).

[32] H. M. Wyss, S. Romer, F. Scheffold, P. Schurtenberger, and L. J. Gauckler, Diffusing-wave spectroscopy of concentrated alumina suspensions during gelation, J. Colloid Interface Sci. **241**, 89 (2001).

[33] F. Gittes and F. C. MacKintosh, Dynamic shear modulus of a semiflexible polymer network, Phys. Rev. E **58**, R1241 (1998).

[34] F. Gittes, B. Schnurr, P. Olmsted, F. C. MacKintosh, and C. F. Schmidt, Microscopic viscoelasticity: Shear moduli of soft materials determined from thermal fluctuations, Phys. Rev. Lett. **79**, 3286 (1997).

[35] A. J. Levine and T. Lubensky, Response function of a sphere in a viscoelastic two-fluid medium, Phys. Rev. E **63**, 041510 (2001).

[36] S. Romer, F. Scheffold, and P. Schurtenberger, Sol-gel transition of concentrated colloidal suspensions, Phys. Rev. Lett. **85**, 4980 (2000).

[37] P. N. Pusey and W. Van Megen, Dynamic light scattering by non-ergodic media, Physica A **157**, 705 (1989).

[38] J.-Z. Xue, D. Pine, S. Milner, X.-L. Wu, and P. Chaikin, Nonergodicity and light scattering from polymer gels, Phys. Rev. A **46**, 6550 (1992).

[39] G. Nisato, P. Hebraud, J.-P. Munch, and S. Candau, Diffusing-wave-spectroscopy investigation of latex particle motion in polymer gels, Phys. Rev. E **61**, 2879 (2000).

[40] A. Knaebel, M. Bellour, J.-P. Munch, V. Viasnoff, F. Lequeux, and J. Harden, Aging behavior of laponite clay particle suspensions, Europhys. Lett. **52**, 73 (2000).

[41] F. Cardinaux, L. Cipelletti, F. Scheffold, and P. Schurtenberger, Microrheology of giant-micelle solutions, Europhys. Lett. **57**, 738 (2002).

[42] V. Viasnoff, F. Lequeux, and D. Pine, Multispeckle diffusing-wave spectroscopy: A tool to study slow relaxation and time-dependent dynamics, Rev. Sci. Instrum. **73**, 2336 (2002).

[43] P. Zakharov, F. Cardinaux, and F. Scheffold, Multispeckle diffusing-wave spectroscopy with a single-mode detection scheme, Phys. Rev. E **73**, 011413 (2006).

[44] K. Pham, S. Egelhaaf, A. Moussaíd, and P. Pusey, Ensemble-averaging in dynamic light scattering by an echo technique, Rev. Sci. Instrum. **75**, 2419 (2004).

[45] S. Zhang, J. Peuser, C. Zhang, F. Cardinaux, P. Zakharov, S. E. Skipetrov, R. Cerbino, and F. Scheffold, Echo speckle imaging of dynamic processes in soft materials, Opt. Express **30**, 30991 (2022).

[46] M. Alexander and D. G. Dalgleish, Diffusing wave spectroscopy of aggregating and gelling systems, Curr. Opin. Colloid Interface Sci. **12**, 179 (2007).

[47] X. Xue, X. Miao, J. Liu, Y. Ding, Y. Zhang, Y. Sun, W. Huang, Q. Jiang, B. Jiang, and S. Komarneni, Investigating the pH-dependence of gelation process in chitosan-glutaraldehyde hydrogels with diffusing wave spectroscopy, Polymer **316**, 127827 (2025).

[48] E. J. Sie, H. Chen, E.-F. Saung, R. Catoen, T. Tiecke, M. A. Chevillet, and F. Marsili, High-sensitivity multispeckle diffuse correlation spectroscopy, Neurophotonics **7**, 035010 (2020).

[49] M. A. Wayne, E. J. Sie, A. C. Ulku, P. Mos, A. Ardelean, F. Marsili, C. Bruschini, and E. Charbon, Massively parallel, real-time multispeckle diffuse correlation spectroscopy using a 500×500 SPAD camera, Biomed. Opt. Express **14**, 703 (2023).

[50] S. E. Skipetrov, J. Peuser, R. Cerbino, P. Zakharov, B. Weber, and F. Scheffold, Noise in laser speckle correlation and imaging techniques, Opt. Express **18**, 14519 (2010).

[51] See Supplemental Material at http://link.aps.org/supplemental/10.1103/k34t-ghws for additional characterization data and figures.

[52] B. Schroyen, D. Vlassopoulos, P. Van Puyvelde, and J. Vermant, Bulk rheometry at high frequencies: A review of experimental approaches, Rheol. Acta **59**, 1 (2020).

[53] G. Fritz, W. Pechhold, N. Willenbacher, and N. J. Wagner, Characterizing complex fluids with high frequency rheology using torsional resonators at multiple frequencies, J. Rheol. **47**, 303 (2003).

[54] K. Schätzel, Noise in photon correlation and photon structure functions, Opt. Acta: Int. J. Opt. **30**, 155 (1983).

[55] J. Yoon, F. Cardinaux, C. Lapointe, C. Zhang, T. G. Mason, K. H. Ahn, and F. Scheffold, Brownian dynamics of colloidal microspheres with tunable elastic properties from soft to hard, Colloids Surf. A **546**, 360 (2018).

[56] P.-A. Lemieux, M. Vera, and D. J. Durian, Diffusing-light spectroscopies beyond the diffusion limit: The role of ballistic transport and anisotropic scattering, Phys. Rev. E **57**, 4498 (1998).

[57] T. G. Mason, Estimating the viscoelastic moduli of complex fluids using the generalized Stokes–Einstein equation, Rheol. Acta **39**, 371 (2000).

[58] R. Evans, M. Tassieri, D. Auhl, and T. A. Waigh, Direct conversion of rheological compliance measurements into storage and loss moduli, Phys. Rev. E **80**, 012501 (2009).

[59] M. Tassieri, R. Evans, R. L. Warren, N. J. Bailey, and J. M. Cooper, Microrheology with optical tweezers: Data analysis, New J. Phys. **14**, 115032 (2012).

[60] M. Tassieri, Comment on "A symmetrical method to obtain shear moduli from microrheology" by K. Nishi, M. L. Kilfoil, C. F. Schmidt, and F. C. Mackintosh, Soft Matter, 2018, 14, 3716, Soft Matter **14**, 8666 (2018).

[61] A. Einstein *et al.*, On the motion of small particles suspended in liquids at rest required by the molecular-kinetic theory of heat, Ann. Phys. **17**, 549 (1905).

[62] E. J. Hinch, Application of the Langevin equation to fluid suspensions, J. Fluid Mech. **72**, 499 (1975).

[63] R. Huang, I. Chavez, K. M. Taute, B. Lukić, S. Jeney, M. G. Raizen, and E.-L. Florin, Direct observation of the full transition from ballistic to diffusive Brownian motion in a liquid, Nat. Phys. **7**, 576 (2011).

[64] I. Madrid *et al.*, Ballistic Brownian motion of nanoconfined DNA, ACS Nano **17**, 17031 (2023).

[65] D. Coglitore, S. P. Edwardson, P. Macko, E. A. Patterson, and M. Whelan, Transition from fractional to classical Stokes–Einstein behaviour in simple fluids, R. Soc. Open Sci. **4**, 170507 (2017).

[66] P. Domínguez-García, F. Cardinaux, E. Bertseva, L. Forró, F. Scheffold, and S. Jeney, Accounting for inertia effects to access the high-frequency microrheology of viscoelastic fluids, Phys. Rev. E **90**, 060301 (2014).

[67] T. Indei, J. D. Schieber, and A. Córdoba, Competing effects of particle and medium inertia on particle diffusion in viscoelastic materials, and their ramifications for passive microrheology, Phys. Rev. E **85**, 041504 (2012).

[68] D. Mizuno, D. Head, F. MacKintosh, and C. Schmidt, Active and passive microrheology in equilibrium and nonequilibrium systems, Macromolecules **41**, 7194 (2008).

[69] *Mathematica*, Version 14.0 (Wolfram Research, Inc., Champaign, IL, 2024).

[70] *Python Language Reference*, version 3.10, Python Software Foundation (Wilmington, Delaware, 2021).

[71] P. Fischer and H. Rehage, Rheological master curves of viscoelastic surfactant solutions by varying the solvent viscosity and temperature, Langmuir **13**, 7012 (1997).

[72] C. Oelschlaeger, M. Schopferer, F. Scheffold, and N. Willenbacher, Linear-to-branched micelles transition: A rheometry and diffusing wave spectroscopy (DWS) study, Langmuir **25**, 716 (2009).

[73] K. Schaetzel and R. Peters, Noise on multiple-tau photon correlation data, in *Photon Correlation Spectroscopy: Multicomponent Systems*, edited by K. S. Schmitz (SPIE, Bellingham, Washington, 1991), Vol. 1430, pp. 109–115.

[74] P. Virtanen, R. Gommers, T. E. Oliphant, M. Haberland, T. Reddy, D. Cournapeau, E. Burovski, P. Peterson, W. Weckesser, J. Bright, S. J. van der Walt, M. Brett, J. Wilson, K. J. Millman, N. Mayorov, A. R. J. Nelson, E. Jones, R. Kern, E. Larson, C. J. Carey *et al.*, SciPy 1.0: Fundamental algorithms for scientific computing in Python, Nat. Methods **17**, 261 (2020).

[75] *CRC Handbook of Chemistry and Physics*, edited by J. Rumble, 106th ed. (CRC Press/Taylor & Francis Group, Boca Raton, FL, 2025).

[76] M. Bergman, Y. Xu, J. Muñéton Díaz, C. Zhang, T. G. Mason, and F. Scheffold, A free energy model for the plateau shear modulus in thermosensitive microgel suspensions, Langmuir **41**, 4084 (2025).

[77] Y. Hertle, M. Zeiser, P. Fouquet, M. Maccarini, and T. Hellweg, The internal network dynamics of poly (NIPAM) based copolymer micro- and macrogels: A comparative neutron spin-echo study, Z. Phys. Chem. **228**, 1053 (2014).

[78] A. Rao, B. R. Carrick, H. Yao, and B. D. Olsen, Hindered segmental dynamics in associative protein hydrogels studied by neutron spin-echo spectroscopy, Phys. Rev. Mater. **7**, 075602 (2023).

[79] H. Manuel, Z. Chi, S. Frank, Expanding the reach of diffusing wave spectroscopy and tracer bead microrheology, [Data set], Zenodo (2025), https://doi.org/10.5281/zenodo.17426137.

[80] https://github.com/ManuelH26/pyDWS.

[81] https://pypi.org/project/pyDWS/.